

Improving the Water Oxidation Efficiency with a Light-Induced Electric Field in Nanograting Photoanodes

Wenrong Wang,^{†,‡,§} Beidou Guo,^{‡,§,#} Haitao Dai,^{//} Chang Zhao,^{‡,§} Guancai Xie,^{‡,§}
Renping Ma,[‡] Muhammad Zain Akram,^{‡,§} Hangyong Shan,[⊥] Congzhong Cai,[†] Zheyu
Fang,^{*,⊥} and Jian Ru Gong^{*,‡,§}

[†]State Key Laboratory of Coal Mine Disaster Dynamics and Control, Department of Applied Physics, Chongqing University, Chongqing 400044, China

[‡]CAS Center for Excellence in Nanoscience, Chinese Academy of Sciences (CAS) Key Laboratory of Nanosystem and Hierarchy Fabrication, National Center for Nanoscience and Technology, Beijing 100190, China

[§]University of CAS, Beijing 100049, China

^{//}Tianjin Key Laboratory of Low Dimensional Materials Physics and Preparing Technology, School of Science, Tianjin University, Tianjin 300072, China

[⊥]School of Physics, State Key Lab for Mesoscopic Physics, Academy for Advanced Interdisciplinary Studies, Collaborative Innovation Center of Quantum Matter, and Nano-optoelectronics Frontier Center of Ministry of Education, Peking University, Beijing 100871, China

Experimental Section

Preparation of Nanograting Photoanodes

1. Synthesis of PS microspheres.

Polystyrene (PS) microspheres were prepared by emulsion polymerization as reported in a previous study.⁶¹ Monodisperse PS dispersions were prepared using sodium lauryl sulfate (SDS) (AR), potassium persulfate (AR), and ethanol (AR) as emulsifier, initiator, and dispersion medium, respectively. Known quantities of sodium lauryl sulfate and potassium persulfate were dissolved in aqueous alcohol in a 250 ml three-neck flask. A certain amount of styrene (CP > 99%), previously washed with 10% sodium hydroxide solution in a separating funnel three times to remove anti-polymerizer, was then added in nitrogen atmosphere rapid stirring, and the emulsion was heated to 70°C and allowed to polymerize for 12 h. After the reaction, the mixed solution was centrifuged and the solid sample was collected and dried at 50°C for 24 h.

2. Preparation of PS microsphere monolayer.

A monolayer of PS microspheres was prepared by the interface method. Briefly, 5 wt% PS microsphere dispersion in a mixture of deionized water and absolute ethanol (v/v, 1:1) along with a tilted silicon piece, was slowly added to deionized water in a 15 cm diameter glass petri dish, then 30 μ L of 2% SDS solution was added. After 6 h, a hydrophilic SiO₂ substrate was immersed in the solution and slowly pulled out of liquid surface to form 2D monolayer of colloidal crystals PS microspheres. The PS microspheres with different diameters (440, 600, and 1000 nm) were used in three different monolayer preparation.

3. Etching SiO₂ with PS microspheres as shadow mask.

SiO₂ FC nanogratings were fabricated by RIE. The RIE process was performed using a mixture of Ar and CF₄ as the processing gas at the total flow rate of 50 sccm, chamber pressure of 0.4 Pa, and RF power of 300 W. Etching time was varied from 120 to 300 s. For the fabrication of non-close-packed SiO₂ FC nanogratings, the PS microspheres were first etched by O₂.

4. Fabrication of ITO/Au/ α -Fe₂O₃ FC nanogratings.

To improve adhesion of the Au layer, a 150 nm ITO adhesion layer was first deposited by magnetic sputtering on the SiO₂ FC. The Au film with the thickness of 100 nm was then deposited on the SiO₂/ITO FC by thermal evaporation. Finally, the Fe film with a certain thickness was magnetically sputtered on the SiO₂/ITO/Au FC.

After annealing at 600 °C for 4 h, SiO₂/ITO/Au/ α -Fe₂O₃ FC nanogratings were successfully obtained.

Characterization of samples

X-ray diffraction (XRD) patterns were recorded using X'pert Powder diffractometer with an operating voltage of 40 kV and 40 mA current, to elucidate the crystal structure of the prepared thin-film photoanodes; grazing incidence XRD (GI-XRD) mode was adopted to increase the signal-to-noise ratio. The micromorphology of the photoanodes was examined by a Hitachi S-4800 field emission scanning electron microscope (FE-SEM) at the accelerating voltage of 10 kV. Ultraviolet-visible (UV-Vis) transmittance and reflectance spectra were recorded using a UV-Vis spectrophotometer (UV-2600) equipped with an external diffuse reflectance accessory (DRA-2500), and the absorptance (A) was calculated using the formula $A=1-T-R$, where T is the total transmittance and R is the total reflectance.

Photoelectrochemical measurements

Photoelectrochemical measurements were carried out using an electrochemical workstation (ZahnerZennium, Germany) in a typical three-electrode configuration with the prepared photoanode as the working electrode, a Pt foil as the counter electrode, a saturated Ag/AgCl electrode (SCE) as the reference electrode, and 1 M NaOH (pH = 13.6) aqueous solution as the electrolyte. Samples with geometrical area of 0.636 cm² were irradiated by a 150 W Xenon lamp (Crowntech. Inc., CT-XE-150) with the light intensity of ~ 450 mW cm⁻². All the measurements were performed with the sample irradiated from the electrolyte side and the angle between the incident light and the electrode was 90°. The photocurrent density versus applied potential (J-V) plots of the photoanodes were traced at the scan speed of 37 mV s⁻¹ in the voltage range between -400 and 600 mV versus SCE. To facilitate comparison between different samples, the measured photocurrent was normalized to the sample's macroscopic area to obtain the photocurrent density (in units of mA cm⁻²); the photocurrent started to rise at the onset potential.

A Si photodiode with known IPCE was used to calculate the IPCE values of the α -Fe₂O₃ photoanodes, and a source meter (Keithley 2400) was used to measure the photocurrents of the Si photodiode and the photoanodes (here the photocurrent of the

photoanodes is obtained by subtracting the dark current from that under irradiation). The IPCE values of the photoanodes were calculated using the following equation:

$$IPCE_{photoanode} = \frac{photocurrent_{photoanode} \times IPCE_{Si}}{photocurrent_{Si}} \quad (1)$$

All the measured potentials against SCE were converted to the reversible hydrogen electrode (RHE) scale according to the Nernst equation:

$$E_{RHE} = E_{Ag/AgCl} + 0.059 \times pH + E_{Ag/AgCl}^0 \quad (2)$$

where E_{RHE} is the calculated potential versus RHE, $E_{Ag/AgCl}$ is the measured potential against the saturated Ag/AgCl electrode, and $E_{Ag/AgCl}^0$ is the standard potential of the saturated Ag/AgCl electrode (0.197 V at 25 °C). IPCE values from 300 to 600 nm were measured at the potential of 0.23 V vs. Ag/AgCl (+1.23 V_{RHE}) using a 150 W Xenon lamp equipped with a monochromator (M24-D).

Theoretical Calculations

All simulations were performed using three-dimensional full-field finite difference time domain methods (Lumerical FDTD Solutions 7.5). The geometrical parameters of the sample were set to be in accordance with the experimental measurement. The cone, FC (200 nm top diameter), and pillar nanograting configurations have the same pitch (600 nm), height (300 nm), and base diameter (440 nm). The disordered FC sample considered has the same pitch, height and diameter (pitch = 600 nm, height = 300 nm, base diameter = 440 nm, top diameter = 200 nm) as the optimized experimental sample. A plane wave light source with wavelength varying in the range 300–1000 nm irradiated perpendicularly incident onto individual FCs with periodic in-plane boundary conditions. All the simulations were carried out with the electrolyte side irradiated, and the mesh accuracy set to be 3, which was proven to be sufficiently fine in convergence tests. Electric field distribution was recorded using two-dimensional field profile monitors. The electric field density in α -Fe₂O₃ layer is obtained by averaging three representative electric field intensity values in the middle and both ends of the strong electric field region inside the α -Fe₂O₃. The field vectors were monitored in three-dimensional grid points to extract the absorption spectra of α -Fe₂O₃ and Au, and to generate field distribution maps at the wavelength of interest.

The total absorbed photon number in different nanograting geometries is calculated using the following equation:

$$N_{absorbed} = \int_{\lambda_a}^{\lambda_b} P(\lambda) A(\lambda) \frac{\lambda}{hc} d\lambda \quad (3)$$

where λ_a is the shortest wavelength of the absorption edge of the photoelectrode; λ_b is the longest wavelength of the absorption edge of the photoelectrode; and P , λ , h , c , and A are the power of incident photons, the wavelength of incident monochromatic light, the Planck constant, the speed of light, and the absorption of the photoelectrode, respectively. Light absorption in the α -Fe₂O₃ and Au layers was calculated using the following equation:

$$P_{abs} = -0.5\omega|E|^2 \text{imag}(\varepsilon) \quad (4)$$

where $\omega = 2\pi/\lambda$ and λ is the irradiation wavelength, E is the electric field intensity, and ε is the Au permittivity. The electric field intensity and Au permittivity were measured by a three-dimensional frequency-domain field monitor and a refractive index monitor, respectively.

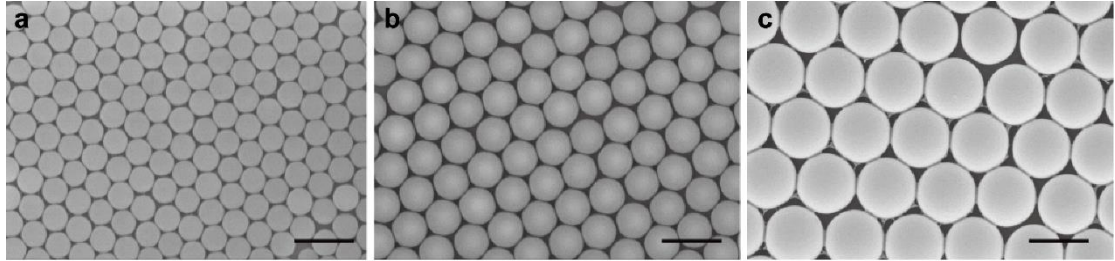


Figure S1. SEM images of monolayers of PS microspheres with different diameters of (a) 440 nm, (b) 600 nm, and (c) 1000 nm. Scale bars, 500 nm.

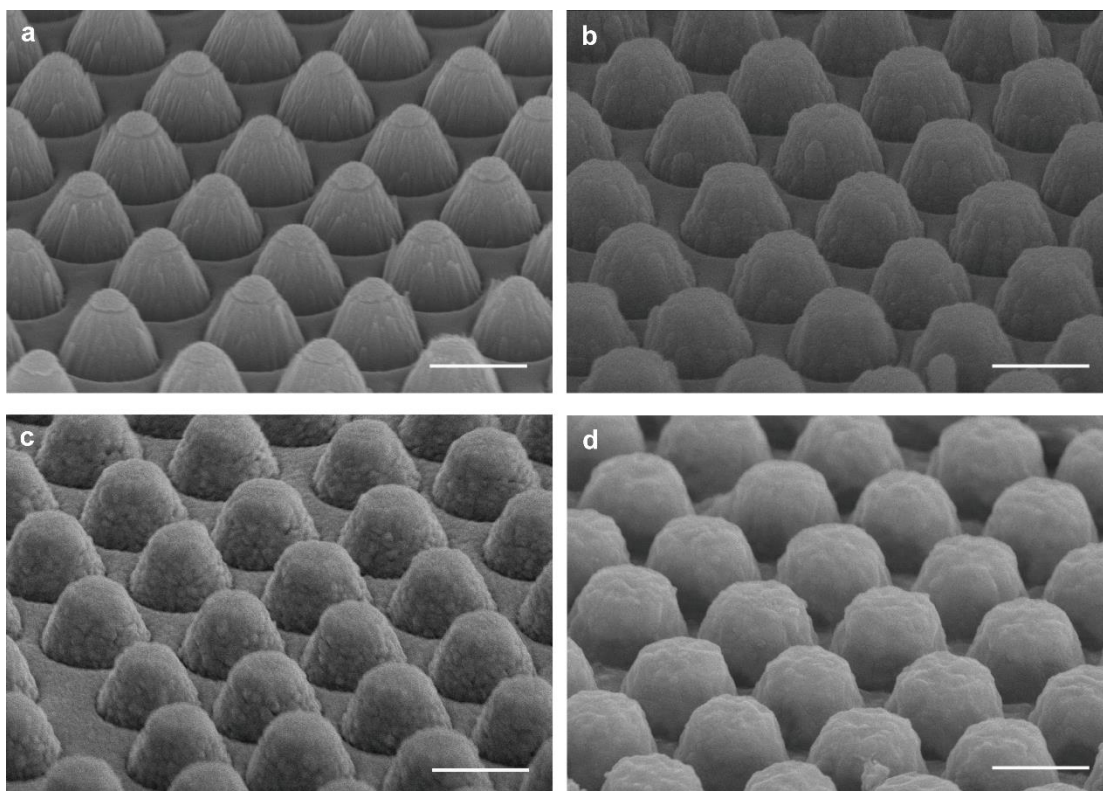


Figure S2. SEM images of the samples at different steps of the photoanode fabrication. SEM images of (a) SiO₂ FC nanograting with the etched PS microsphere on the top of each FC; (b) SiO₂ FC nanograting with a 150 nm-thick ITO adhesion layer after washing the PS microspheres; (c) ITO-coated SiO₂ FC nanograting after thermally depositing a 100 nm-thick Au film; (d) SiO₂/ITO/Au FC nanograting with a 50 nm-thick Fe film magnetically sputtered after annealing at high temperature. Scale bars, 500 nm.

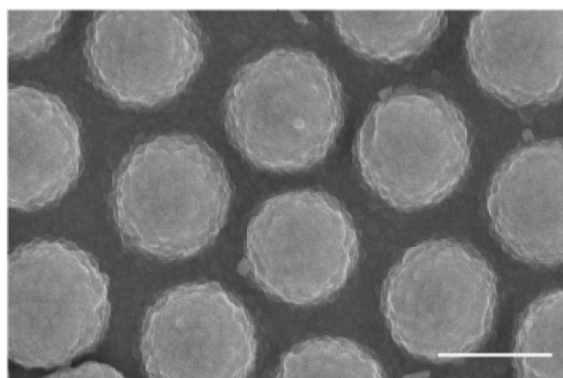


Figure S3. Top-view SEM image of the ordered SiO₂/ITO/Au/ α -Fe₂O₃ FC nanograting (pitch = 600 nm, height = 300 nm, base diameter = 440 nm, and top diameter = 200 nm). The scale bar is 500 nm.

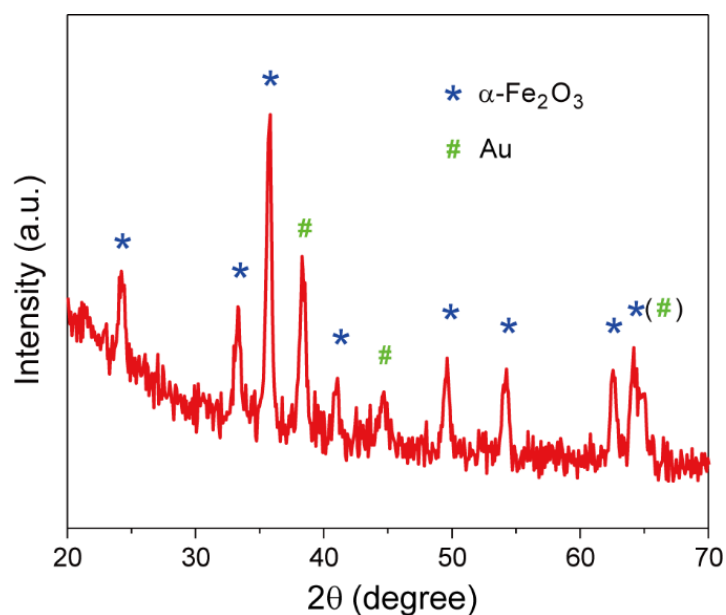


Figure S4 . XRD pattern of the as-prepared $\text{SiO}_2/\text{ITO}/\text{Au}/\alpha\text{-Fe}_2\text{O}_3$ anode with the FC nanograting structure.

The X-ray diffraction (XRD) pattern in Figure S4 shows characteristic peaks corresponding to diffraction from the (012), (104), (110), (113), (024), (116), (214), and (300) planes of $\alpha\text{-Fe}_2\text{O}_3$ (PDF # 33-0664), indicating complete conversion from Fe to $\alpha\text{-Fe}_2\text{O}_3$; (111), (200), and (220) peaks for Au (PDF # 04-0784) are also detected, confirming the successful deposition of the Au film.

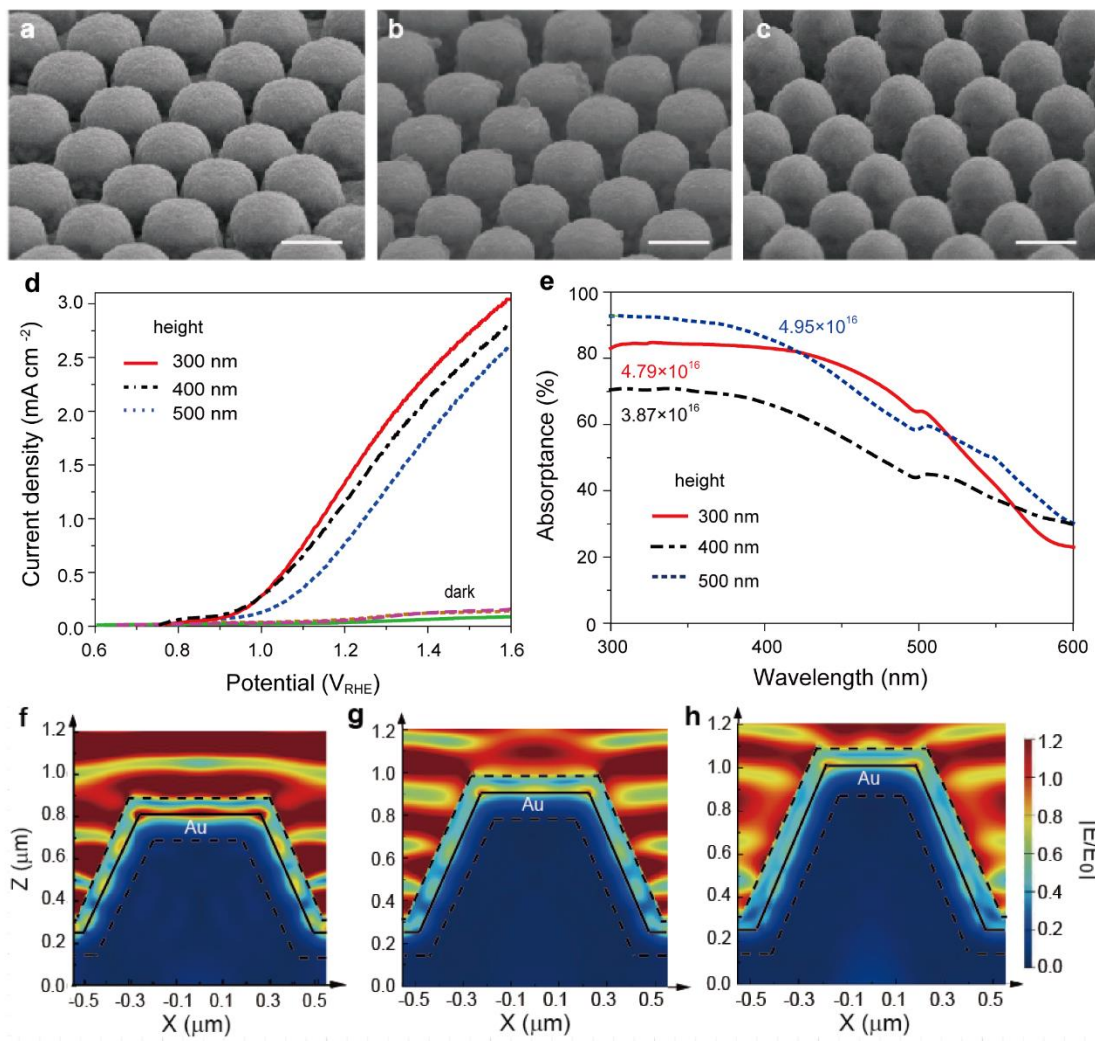


Figure S5. SiO₂/ITO/Au/α-Fe₂O₃ FC nanogratings with different heights. SEM images of SiO₂/ITO/Au/α-Fe₂O₃ FC nanogratings with different heights, (a) 300 nm, (b) 400 nm, and (c) 500 nm. Scale bars, 500 nm. (d) Photocurrent and dark current densities of SiO₂/ITO/Au/α-Fe₂O₃ FC nanogratings of different heights. (e) FDTD simulated absorption curves of α-Fe₂O₃ in SiO₂/ITO/Au/α-Fe₂O₃ FCs with different heights (300, 400, and 500 nm). The total absorbed photon number in 300-600 nm is labeled on the corresponding curve, respectively. FDTD-simulated electric field distribution $|E/E_0|$ of SiO₂/ITO/Au/α-Fe₂O₃ FCs with different heights, (f) 300 nm, (g) 400 nm, and (h) 500 nm at the wavelength of 516 nm.

First, the changes of the photocurrent, absorption, FDTD-simulated electric field intensity of the $\text{SiO}_2/\text{ITO}/\text{Au}/\alpha\text{-Fe}_2\text{O}_3$ anode with the different FC nanograting heights (300, 400, and 500 nm) and the same pitch (600 nm) and base diameter (440 nm) were studied (Figure S5a-c). The photocurrent density of $\text{SiO}_2/\text{ITO}/\text{Au}/\alpha\text{-Fe}_2\text{O}_3$ decreases in the whole tested potential range when the height increases (Figure S5d). In contrast, light absorption of $\alpha\text{-Fe}_2\text{O}_3$ increases with increasing height (Figure S5e, Table 1), implying that light absorption is not the main reason for the photocurrent decrease. The electric field intensity in $\alpha\text{-Fe}_2\text{O}_3$ near the $\text{Au}/\alpha\text{-Fe}_2\text{O}_3$ interface decreases with increasing height (Figure S5f-h), which is in accordance with the experimentally observed changing trend in photocurrent density, indicating the electric field intensity is closely related to the anode activity (Table 1).

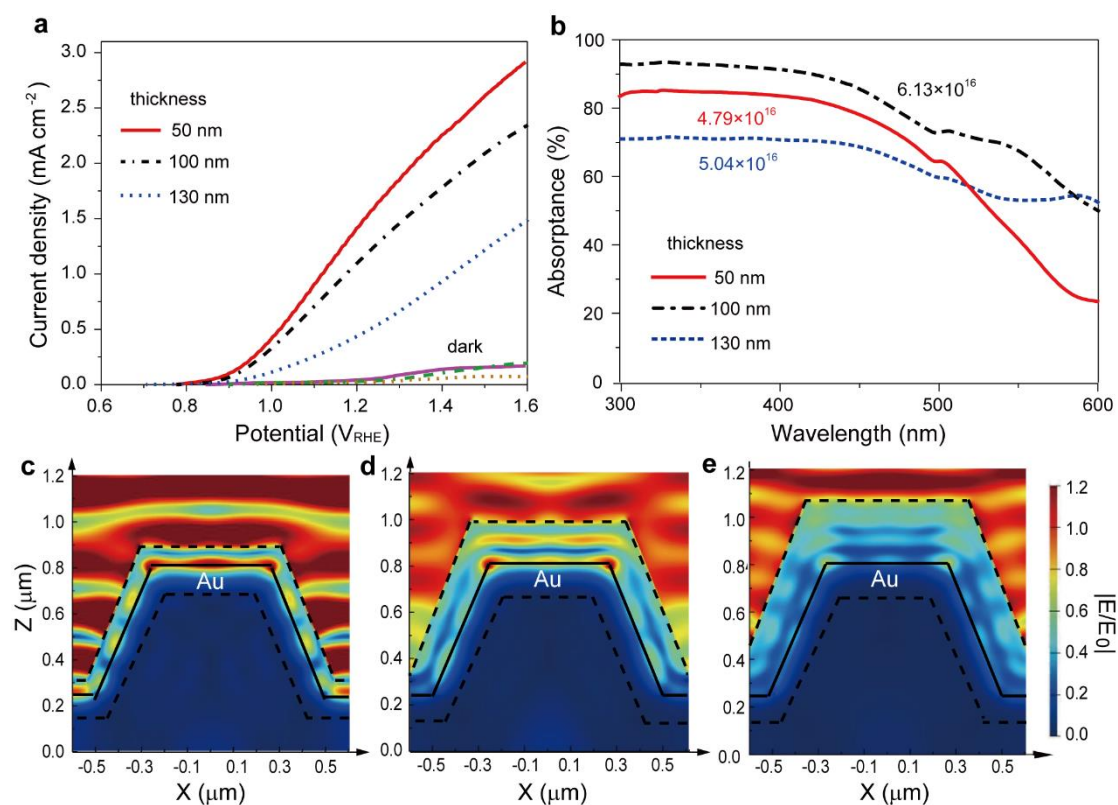


Figure S6. $\text{SiO}_2/\text{ITO}/\text{Au}/\alpha\text{-Fe}_2\text{O}_3$ FC nanogratings with different $\alpha\text{-Fe}_2\text{O}_3$ thicknesses. (a) Photocurrent and dark current densities of $\text{SiO}_2/\text{ITO}/\text{Au}/\alpha\text{-Fe}_2\text{O}_3$ FC nanogratings with different $\alpha\text{-Fe}_2\text{O}_3$ thicknesses. (b) FDTD simulated absorption curves of $\alpha\text{-Fe}_2\text{O}_3$ in $\text{SiO}_2/\text{ITO}/\text{Au}/\alpha\text{-Fe}_2\text{O}_3$ FCs with different thicknesses (50, 100, and 130 nm). The

total absorbed photon number in 300-600 nm is labeled on the corresponding curve, respectively. FDTD-simulated electric field distribution $|E/E_0|$ of $\text{SiO}_2/\text{ITO}/\text{Au}/\alpha\text{-Fe}_2\text{O}_3$ FCs with different $\alpha\text{-Fe}_2\text{O}_3$ thicknesses, (c) 50 nm, (d) 100 nm, and (e) 130 nm at the wavelength of 516 nm.

Due to the subwavelength thickness of the $\alpha\text{-Fe}_2\text{O}_3$ layer, the effective refractive index is averaged over the $\alpha\text{-Fe}_2\text{O}_3$ layer and the electrolyte.¹⁻³ So we change the $\alpha\text{-Fe}_2\text{O}_3$ layer thickness to adjust the effective refractive index to get better SPP. With increasing $\alpha\text{-Fe}_2\text{O}_3$ layer thickness (50 nm, 100 nm, and 130 nm), the photocurrent density reduces gradually (Figure S7a). As shown in Figure S7b, the FC nanograting with the $\alpha\text{-Fe}_2\text{O}_3$ thickness of 100 nm obtains the maximum total absorbed photon number in $\alpha\text{-Fe}_2\text{O}_3$ by FDTD simulation at the wavelength range of 300–600 nm, meaning the maximum light absorption in $\alpha\text{-Fe}_2\text{O}_3$. Thus, the activity change with thickness cannot be explained by change of absorption (Figure S7b, Table 1). In contrast, the electric field in the $\alpha\text{-Fe}_2\text{O}_3$ layer decreases with $\alpha\text{-Fe}_2\text{O}_3$ thickness (Figure S7c-e), which is in accordance with the changing trend in the photocurrent density.

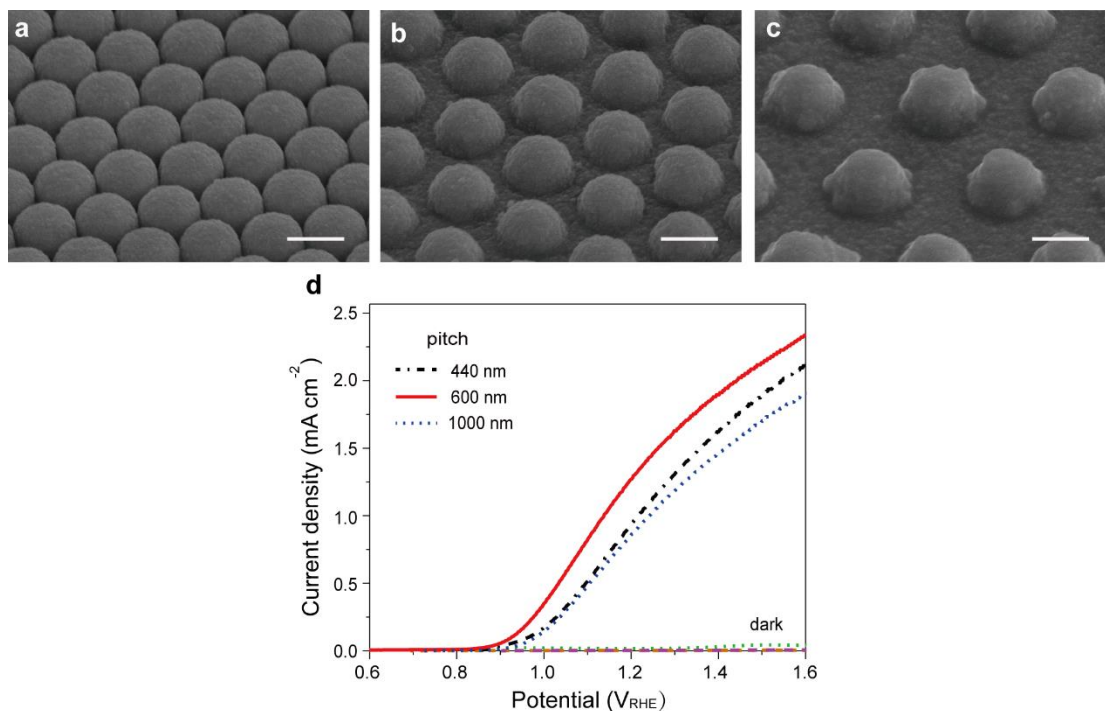


Figure S7. SiO₂/ITO/Au/α-Fe₂O₃ FC nanogratings with different pitches. SEM images of the SiO₂/ITO/Au/α-Fe₂O₃ FC nanogratings with different pitches, (a) 440 nm, (b) 600 nm, and (c) 1000 nm. The scale bars, 500 nm. (d) Photocurrent and dark current densities of SiO₂/ITO/Au/α-Fe₂O₃ FC nanogratings with different pitches (440, 600, and 1000 nm).

We also optimized for the pitch (440, 600, and 1000 nm) of the FC nanograting for the better activity of the photoanodes, with all other parameters remaining the same (Figure S7a-c). The maximum photocurrent density of ~1.33 mA cm⁻² at the bias of 1.23 V_{RHE} is obtained when the pitch of the FC nanograting is 600 nm (Figure S7d). We did not do the FDTD simulation for different pitched, because our simulation conditions cannot meet such a large calculating requirement.

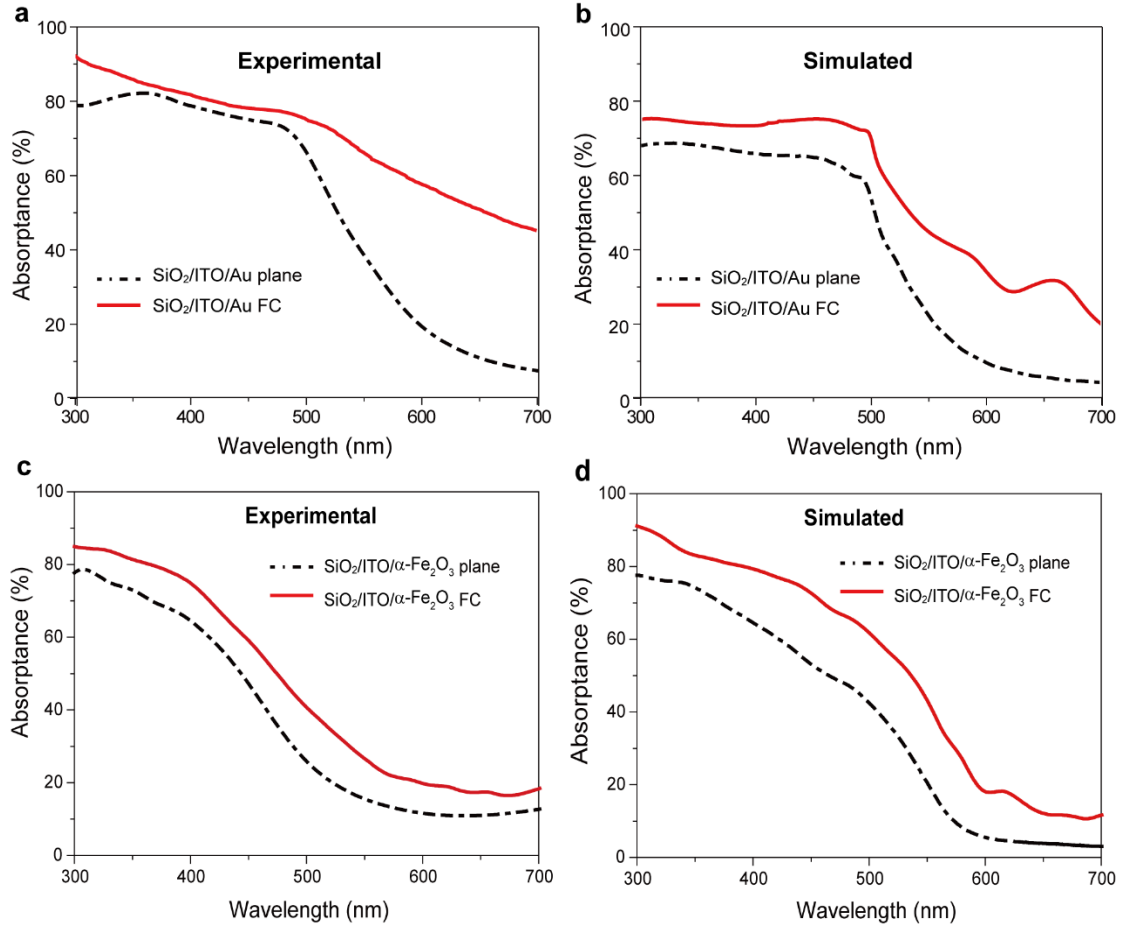


Figure S8. Light absorption spectra of $\text{SiO}_2/\text{ITO}/\text{Au}$ and $\text{SiO}_2/\text{ITO}/\alpha\text{-Fe}_2\text{O}_3$ FC nanograting and planar structures. (a) Experimental and (b) simulated light absorption spectra of $\text{SiO}_2/\text{ITO}/\text{Au}$ FC nanograting (pitch = 600 nm, height = 300 nm, base diameter = 440 nm, and top diameter = 200 nm) and planar structures. (c) Experimental and (d) simulated light absorption spectra of $\text{SiO}_2/\text{ITO}/\alpha\text{-Fe}_2\text{O}_3$ FC nanograting (pitch = 600 nm, height = 300 nm, base diameter = 440 nm, and top diameter = 200 nm) and planar structures.

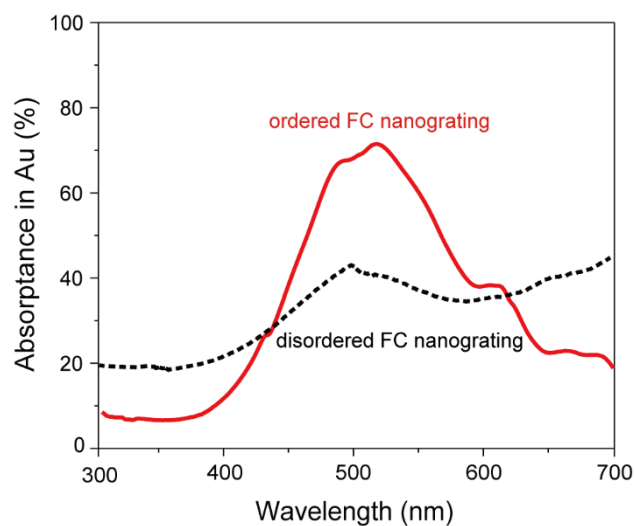


Figure S9. FDTD simulated absorption curves of Au in the ordered and disordered FC nanogratings of SiO₂/ITO/Au/α-Fe₂O₃.

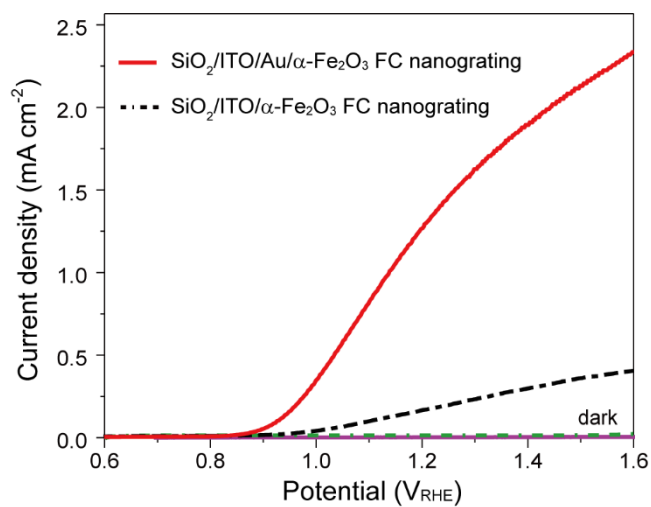


Figure S10. Photocurrent and dark current densities of SiO₂/ITO/Au/α-Fe₂O₃ and SiO₂/ITO/α-Fe₂O₃ (without Au) FC nanograting structures.

Table S1. Comparison of PEC OER of the Au/Fe₂O₃ Based Photoanodes.

Photoanode	Mechanism of plasmon	Electrolyte	Maximum relative IPCE ^a	Reference
SiO ₂ /ITO/Au/Fe ₂ O ₃ FC nanograting	SPP-induced electric field	1 M NaOH	110	our work
Fe ₂ O ₃ electrodes on Au nanopillar array	SPR light absorption	1 M NaOH	4	5
Au/Fe ₂ O ₃ nanoplates	LSPR hot electron injection	1 M KOH	2.5	6
Fe ₂ O ₃ on SiO ₂ /Au/Ti nanohole array	SPP guided mode, increasing absorption; LSPR increased absorption	1 M NaOH	18	7
Fe ₂ O ₃ film embedded with Au nanoparticles	LSPR increased Light absorption	0.5 M NaOH	2	8

^a The incident photon-to-current efficiency.

Table S1 lists a literature survey of some representative publications of the Au/Fe₂O₃ based photoanodes for the plasmonic enhancement of the PEC OER. The relative IPCE of the sample was used for the performance comparison since it can accurately display the plasmonic effect. The relative IPCE value of our sample shows a dramatic ~110-fold increase at 516 nm. In contrast, no more than 20-fold increase was reported in the related works. That is, our relative IPCE value is about 6-55 times higher than those reported for the Au/Fe₂O₃ based photoanodes. demonstrating the highest enhancement factor reported so far.

References

- (1) Zhang, J.; Chen, Z.; Wang, Z.; Zhang, W.; Ming, N. *Mater. Lett.* **2003**, 57, (28), 4466-4470.
- (2) Gao, H.; Liu, C.; Jeong, H. E.; Yang, P. *ACS Nano* **2012**, 6, (1), 234-240.
- (3) Raether, H. *Springer Tracts in Modern Physics* **1988**, 111, 1-133.
- (4) Chien, F. C.; Chen, S. J. *Opt. Lett.* **2006**, 31, (2), 187-189.
- (5) Gao, H.; Liu, C.; Jeong, H. E.; Yang, P. *ACS Nano* **2012**, 6, (1), 234-240.
- (6) Lei, F.; Liu, H.; Yu, J.; Tang, Z.; Xie, J.; Hao, P.; Cui, G.; Tang, B. *Phys. Chem. Chem. Phys.* **2019**, 21, (3), 1478-1483
- (7) Li, J.; Cushing, S. K.; Zheng, P.; Meng, F.; Chu, D.; Wu, N. *Nat. Commun.* **2013**, 4, 2651-2658.
- (8) Archana, P. S.; Pachauri, N.; Shan, Z. C.; Pan, S. L.; Gupta, A. *J. Phys. Chem. C* **2015**, 119, (27), 15506-15516.